SECTION 8

MICROWAVE EMISSION MEASUREMENTS OF SEA SURFACE ROUGHNESS, SOIL MOISTURE, AND SEA ICE STRUCTURE

by

P. Gloersen, T. Wilheit, and T. Schmugge
Laboratory for Meteorology
and Earth Sciences
Goddard Space Flight Center
Greenbelt, Maryland 20771

In order to demonstrate the feasibility of the microwave radiometers to be carried aboard the Nimbus V and VI satellites and proposed for one of the Earth Observatory Satellites, remote measurements of microwave radiation at wavelengths ranging from 0.8 to 21 cm have been made of a variety of the Earth's surfaces from the NASA CV-990 A/C. The instrument complement has been described elsewhere[1]. Brightness temperatures of sea water surfaces of varying roughness, of terrain with varying soil moisture, and of sea ice of varying structure were observed. In each case, surface truth information was available for correlation with the microwave brightness temperature. Radiation at 1.55 cm was mapped with an image-forming radiometer over these areas, while radiation at the other wavelengths was measured at fixed viewing angles with respect to the aircraft, primarily to determine the wavelength dependence of the phenomena mapped at 1.55 cm.

The physical basis for the interpretation of such measurements is given by the equation shown in Figure 1. In this wavelength region, the Rayleigh-Jeans approximation holds for all cases of interest, therefore the signal received by the radiometer is proportional to the brightness temperature of the source. The surface contribution is shown in the brackets; it is reduced before arriving at the radiometer by the atmospheric transmissivity, τ. It consists of an emission term given by the product of the emissivity and thermometric temperature of the surface, and a reflection term given by the product of the surface reflectivity, or one minus the emissivity, times the sky temperature as viewed from the surface, averaged over the hemisphere. The last term is the contribution from the atmosphere, as viewed from the spacecraft or aircraft; it is negligible for the low altitude data to be discussed in this paper. We shall concentrate on only one of the factors shown in this equation, the emissivity ε, which is a function of the wavelength λ, the look angle β, and various surface characteristics i.

The general nature of such surface characteristics variation is illustrated in Figure 2 for the measurements to be discussed here. In each case we have plotted the emissivity normal to the surface as a function of frequency in gHz : a few select wavelengths are indicated on the abscissa for reference. For the ocean surface, the effect of surface winds disturbing the sea is to increase the emissivity of the surface. In the case of terrain, the effect of wetting unvegetated soil is to lower the emissivity of the surface; heavily vegetated terrain is uniformly high in emissivity over a wide range of moisture conditions in the soil. For sea ice, first year thick sea ice is a glossy medium which has high emissivity as long as the thickness exceeds one wavelength, that is, as long as it is optically thick. Multi-year ice, on the other hand, is a good dielectric, and would be quite transparent to the microwaves except for the presence of many scattering centers such as unfilled brine cells; thus, it becomes a good diffuse reflector and, therefore, a poor emitter at least at the shorter wavelengths. First year thin ice, that is, less than a wavelength thick, represents a third type for which the emissivity lies somewhere in between and the thick first year ice curve, depending on the thickness of the ice. The calm sea curve is repeated on this graph. Intermediate emissitivies are, of course, obtained also when open water is observed in the ice pack in non-beam-filling situations, but of course, in all channels at once, as opposed to the wavelength dependences seen when viewing various ice types. In the remainder of the paper, we shall be a bit more quantitative in discussing these various pheonmena.

Let us discuss sea ice in more detail. Figure 3 is a view of the Point Barrow, Alaska, test area, showing sea ice as blue or yellow, snow-covered terrain as white or pink, and open water as black, in the order of decreasing brightness temperature. Further north, on the Arctic ice canopy, two different types of sea ice were observed, as shown in Figure 4. This is the same area Bill Campbell discussed in an earlier paper at this meeting, describing the activities at AIDJEX Camp 200, located near the center of this image. This view is a computer-produced mosaic of five separate parallel tracks flown by the aircraft over the test area at an altitude of 10 km: the area shown is about 70 x 80 km in extent. The two ice types shown here are first year thick, as indicated by the yellow and orange colors, and multi-year, as indicated by the blues; we have a high degree of confidence in this interpretation in view of the surface observations available to us thru the AIDJEX activities. The large multi-year ice floe on which Camp 200 was located can be seen to be segmented into three large pieces, separated by first year ice in the refrozen leads. Evidently, this large flow had begun to break up late in the last summer season, but had been frozen into this position by the formation of new ice. A refrozen polynya can be seen at the apex of the inverted v-shaped pattern of the refrozen leads.

Very close scrutiny of the high altitude photography revealed the presence of these features also, thereby supporting this interpretation. With the total cloud cover common to this area, it would, of course, be impossible to see the surface visually, with photography, or, for that matter, infrared or visible imagery in general. On the following day, the area was completely covered by clouds. However, on that next day, the microwave view of the area was substantially unchanged, as shown in Figure 5. If you look closely you can also see about an 8° shift in temperature between these two scenes; as we found out on our low-level passes, this was mostly due to a corresponding change in surface temperature. Some multi-spectral data were obtained for these two ice types as the aircraft took a low altitude pass starting in the northeast quadrant of the scene, passing over the AIDJEX and crossing the ice floe in a southwesterly direction. The results are shown in Figure 6. The edges of the ice floe are clearly shown; the spikes appearing on the ice floe data result from a leg of the v-shaped refrozen lead (actually several refrozen leads when viewed at the higher resolution shown here). As indicated earlier, the contrasts of this particular feature diminish with frequency. Our on-board infrared radiometer indicated surface temperatures to be constant within $\pm$ 5°K over a good portion of this track, independent of ice type and in agreement with thermometric measurements of Camp 200. Figure 7 shows evidence of a third type of ice, first year thin. The ice represented by the largest dip at 1.42 gHz is the order of a wavelength thick, or less, so that the ocean water can be partly seen through the sea ice; in this particular example, the ice was evidently the order of 10 cm thick, since the shorter wavelengths show no corresponding decreases in brightness temperature. As you can see, this effect diminishes as frequency increases; for the 1.42 gHz or 21 cm case, the largest dip shown goes about half way to the calm sea limit; at a wavelength of 11 cm, the same feature dips only about 1/4 of the way. The rough estimate of ice thickness quoted is based on the assumption that the e-folding length of the absorption in the ice is about a wavelength. Careful inspection reveals that the dips shown at longest wavelengths correspond to small peaks at the shortest wavelengths; these were identified from the 1.55 cm image of the area as first year ice between patches of small multi-year floes.

Next we will discuss the changes in emissivity resulting from variations of soil moisture. The image formed from the data obtained during a low altitude pass over an agricultural area near Phoenix, Arizona is shown in Figure 8. In spite of the image distortion resulting from the low altitude of the pass and the low scan rate, the pattern of the individual cultivated fields can be recognized in the rectangular patterns displayed here. Dry fields are indicated as red rectangles,

very wet fields as black rectangles, and intermediate cases as yellow, green, and blue. A more quantitative presentation of such data is given in Figure 9, obtained from one of the other radiometers at a fixed viewing angle. Here the brightness temperature is plotted against the percent soil moisture by weight. According to the on-board infrared radiometer, the surface temperature corresponding to these data was 291°K, with a maximum deviation of + or -4K, hence the maximum emissivity, at the inqercept, is about 0.96. The summary of this and some data taken at other wavelengths is shown in Table I. Noteworthy here is the gradual decrease in slope with the decrease in wavelength and an uncertainty in the brightness temperature at a given moisture content of 5 - 6K. The variation in the intercept is more due to errors in the absolute temperature calibrations of each instrument than anything else.

We now change the topic to some sea surface observations, taken entirely at the 1.55 cm wavelength. These results have been published but they are included here for the sake of completeness. The observations are summarized on the graph shown in Figure 10, where we have plotted brightness temperature changes vs. sea surface winds. As can be seen, the brightness temperature, and hence the emissivity, was observed to increase linearly with wind speed at the surface above a threshold of about 7 m/sec. This increase has been interpreted to be due largely to the presence of foam to varying extent at wind speeds above this threshold, as indicated by the data in the Figure 11. The segments of data shown here are for increasing wind speed, going from left to right. The large spikes that appear with increasing frequency as the wind speed, or average brightness temperature, increases are <u>not</u> noise spikes, but are due to small patches of foam, observed also on the photographs of the sea surface taken at the same time. In Figure 12 the correlation betwee the % foam cover measured from photographic data and the radiometric data is shown. Again, the relationship is linear, within the available measuring accuracy. For comparison, we show also a straight line from the origin to a data point obtained from a foam patch that was 100% beam-filling, along the lower part of which the results of some computations from Cardone's whitecap model also fall.

In summary, we have demonstrated the utility of passive microwave radiometry in determining ocean surface wind speeds, at least for values higher than 7 meters per second. In addition, we have shown that such radiometric signatures have been used to determine soil moisture in unvegetated terrain to within five percentage points by weight. Finally, it has been shown that we can distinguish between first year thick, multi-year, and first year thin sea ice by observing their differing microwave emissivities at various wavelengths. We can also determine the extent of sea ice coverage in the polar ice canopies; the amount of open water present in the Arctic polar ice canopy apparently

has profound effects on the long-term weather in our part of the Northern Hemisphere[1,3,4].

Our future plans include continuation of these aircraft missions to improve our data base, and initiating satellite-borne instrumentation to extend our studies to a global scale. In 1973, we are scheduled to fly a 1.55 cm imager on Nimbus V; a year later, a 0.8 cm imager with dual polarization and constant incidence angle is scheduled to be carried on Nimbus VI. Beyond that, we are working on a multichannel microwave radiometer covering the wavelength range from 0.8 to 6 cm to be flown on the follow-ons to the Nimbus and ERTS satellite series, and on tehcniques for improving the present surface resolutions with a multi-beam approach.

REFERENCES

1. T. Wilheit, J. Blinn, W. Campbell, A. Edgerton, and W. Nordberg, "Aircraft Measurements of Microwave Emission from Arctic Sea Ice", to be published in Remote Sensing of Environment (1972).

2. W. Nordberg, J. Conaway, D. B. Ross, and T. Wilheit, "Measurements of Microwave Emission from a Foam-Covered, Wind-Driven Sea", J. Atmos. Sci., 28, 429-435 (1971).

3. F. I. Badgley, "Heat Budget at the Surface of the Arctic Ocean", Proc. of the Symp. on the Arctic Heat Budget and Atmospheric Circulation, edited by J. O. Fletcher, The Rand Corporation (RM-5233-NSF) (1966).

4. W. Wittmann and J. Schule, "Comments on the Mass Budget of Arctic Pack Ice", Proc. of the Symp. on the Arctic Heat Budget and Atmospheric Circulation, edited by J. O. Fletcher, The Rand Corporation (RM-5233-NSF) (1966).

Table I

LINEAR REGRESSION RESULTS
MICROWAVE BRIGHTNESS TEMPERATURE
VS
SOIL MOISTURE CONTENT

WAVELENGTH	INTERCEPT	SLOPE	STANDARD ERROR OF ESTIMATE
21 CM	280	-2.22	6.22
6 CM	307	-1.65	5.46
1.55 CM	281	-1.44	4.34.
0.8 CM	292	-1.16	5.50

$$T_{B_{H,V}} = \tau_o \left\{ \epsilon_{H,V}(\lambda, \beta, \gamma_i) T_T + \left[1 - \epsilon_{H,V}(\lambda, \beta, \gamma_i) \right] \overline{T}_{B_{SKY}} \right\} + T_{B_{ATM}}$$

- $T_{B_{H,V}}$: OBSERVED RADIOMETRIC TEMPERATURE
- τ_o: ATMOSPHERIC TRANSMISSIVITY
- $\epsilon_{H,V}(\lambda, \beta, \gamma_i) T_T$: THERMAL CONTRIBUTION FROM SURFACE
- $\left[1 - \epsilon_{H,V}(\lambda, \beta, \gamma_i) \right] \overline{T}_{B_{SKY}}$: REFLECTED CONTRIBUTION FROM SURFACE (SKY SOURCE)
- $T_{B_{ATM}}$: DIRECT ATMOSPHERIC CONTRIBUTION

$$\left(T_{B_{ATM}} = \int_0^{h_\infty} T_{T_{ATM}}(h) \frac{\partial \tau}{\partial h} \, dh \right)$$

Figure 1 **Microwave brightness temperature as a function of several variables**

SPECTRAL CHARACTERISTICS OF VARIOUS SURFACES

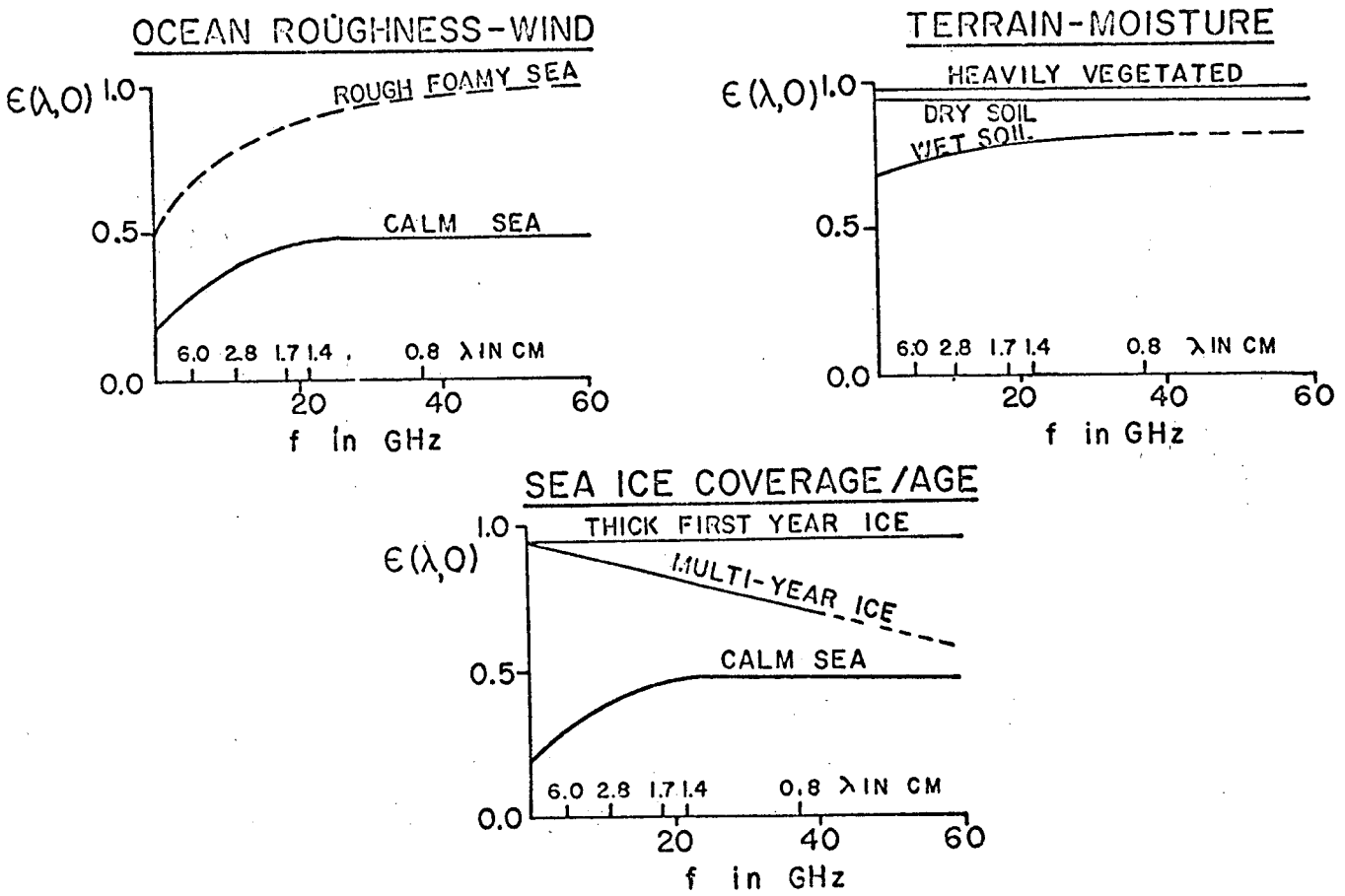

Figure 2 Spectral variations of the emissivity of various surfaces

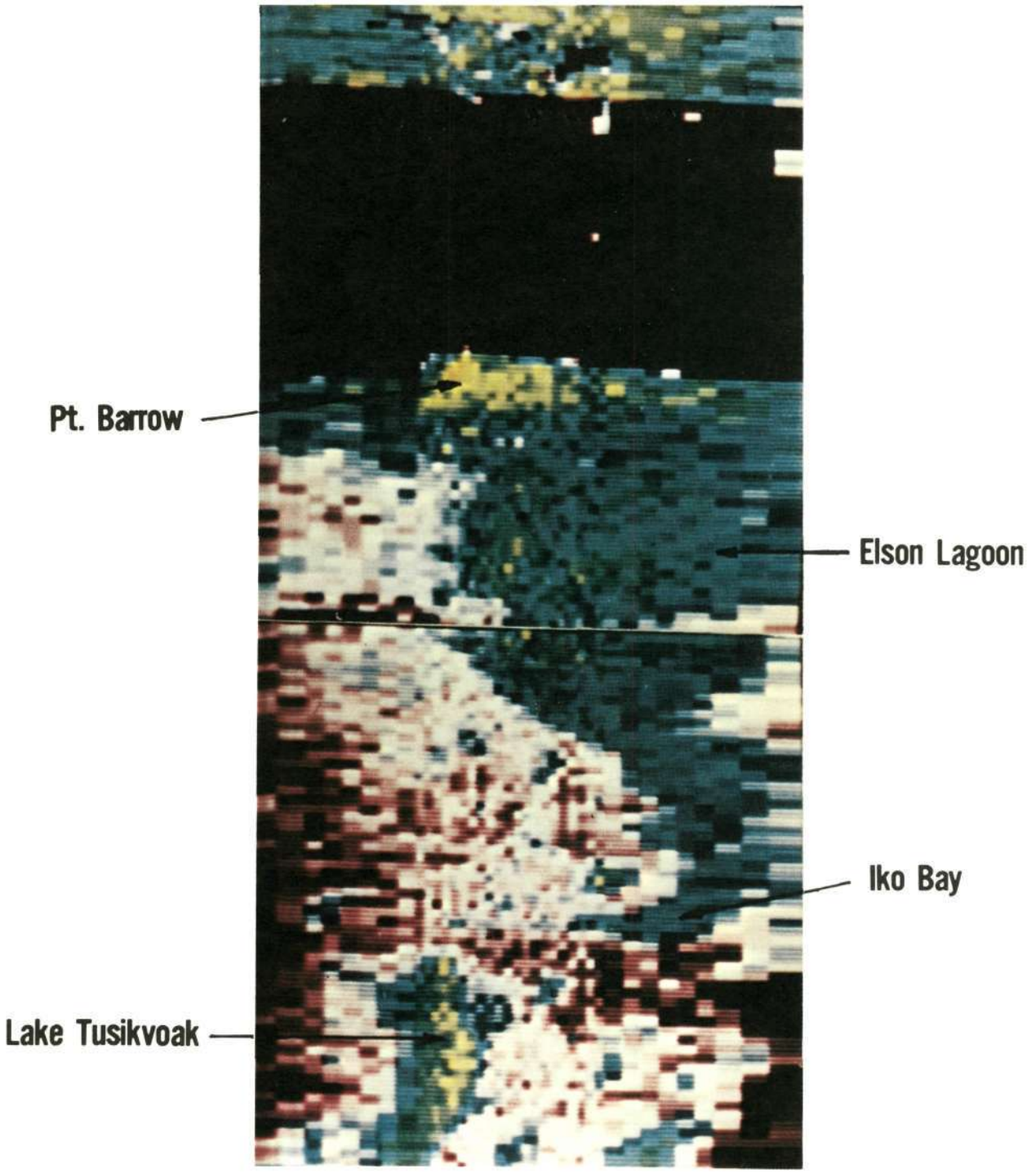

Figure 3 19.35 GHz image of the Point Barrow Test Area

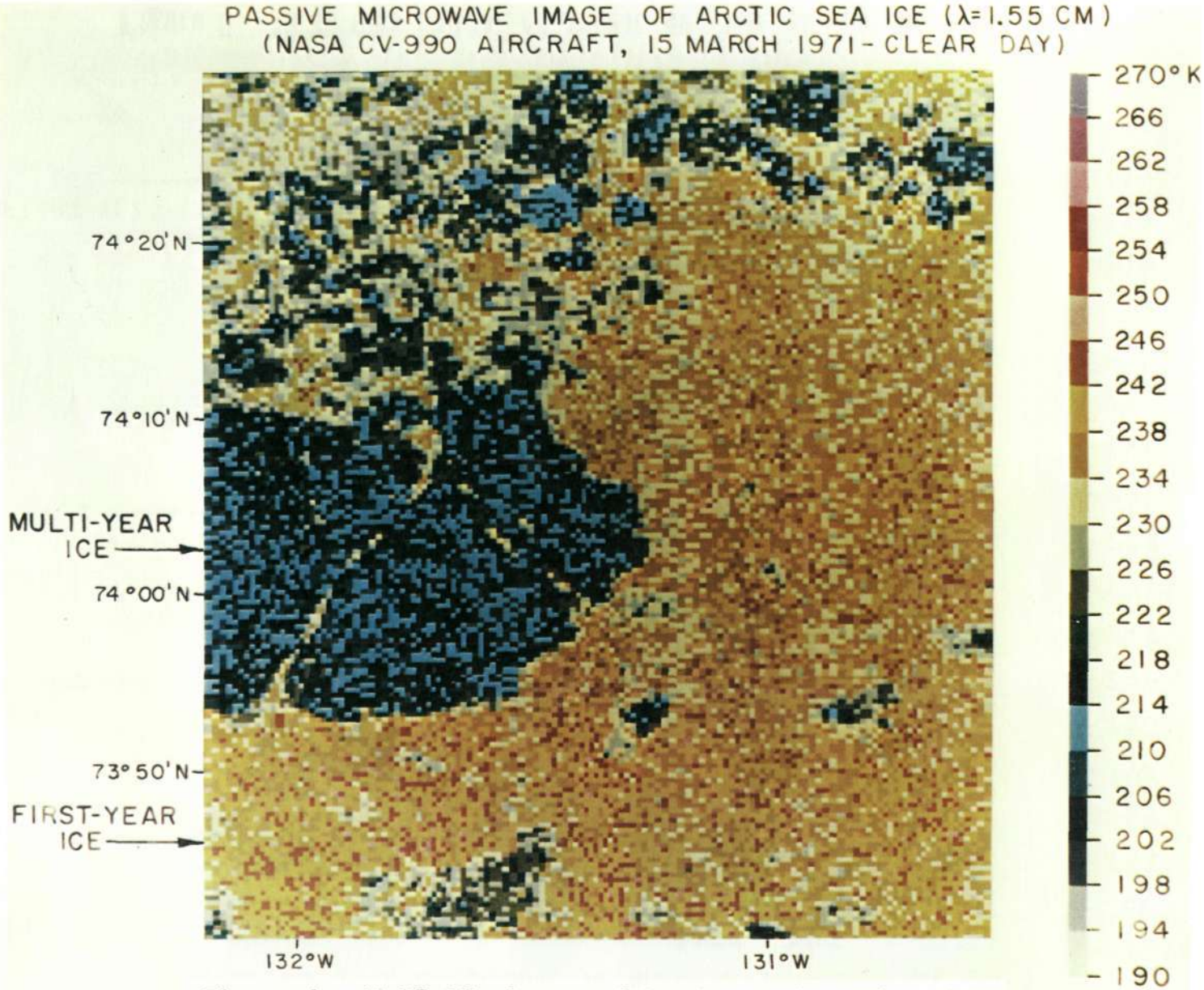

Figure 4 19.35 GHz image of Arctic sea ice, clear day

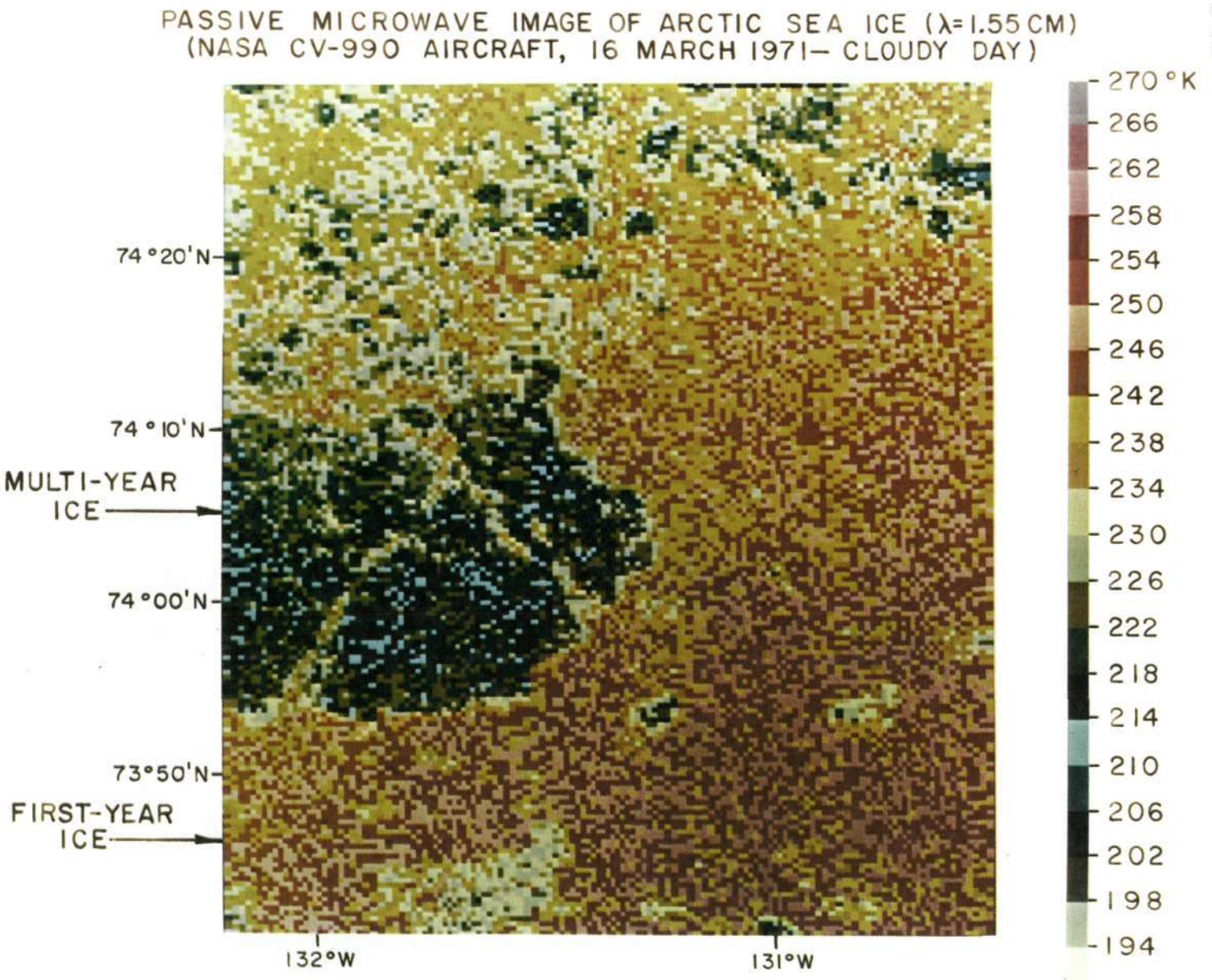

Figure 5 19.35 GHz image of Arctic sea ice, cloudy day

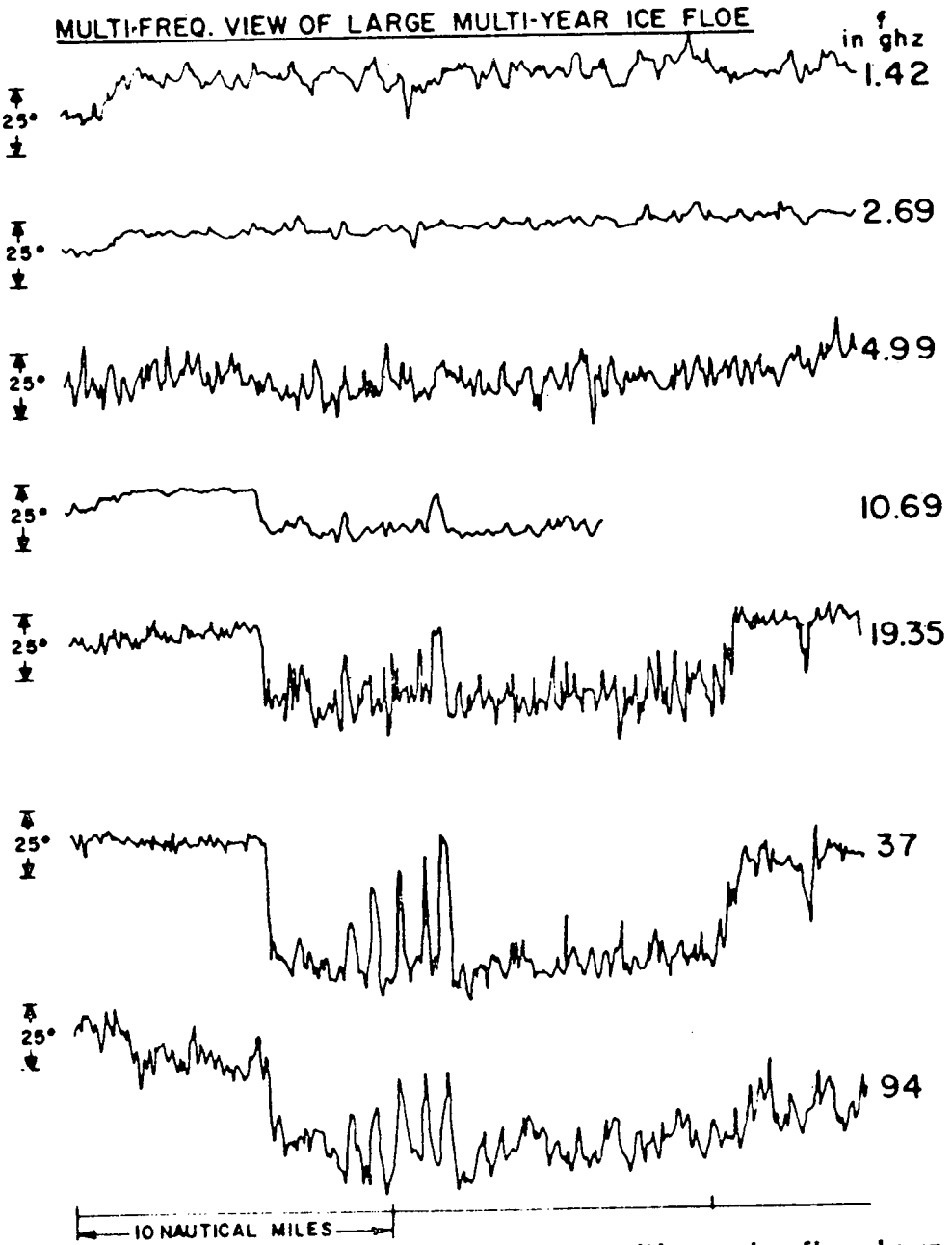

Figure 6 Multispectral view of the large multiyear ice floe shown in Figures 4 & 5; low-altitude pass in a southwesterly direction

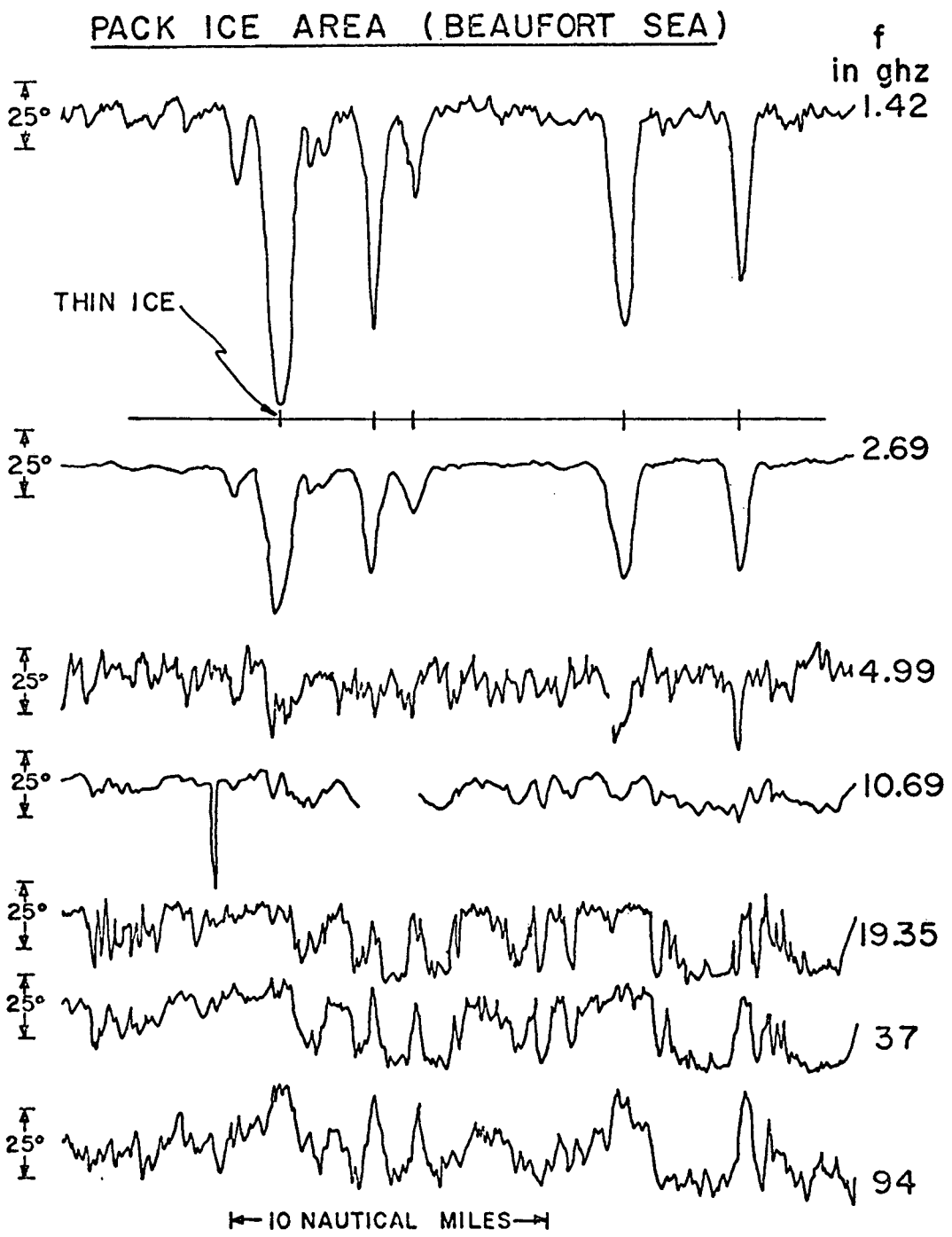

Figure 7 Multispectral view of sea-ice in the Beaufort Sea

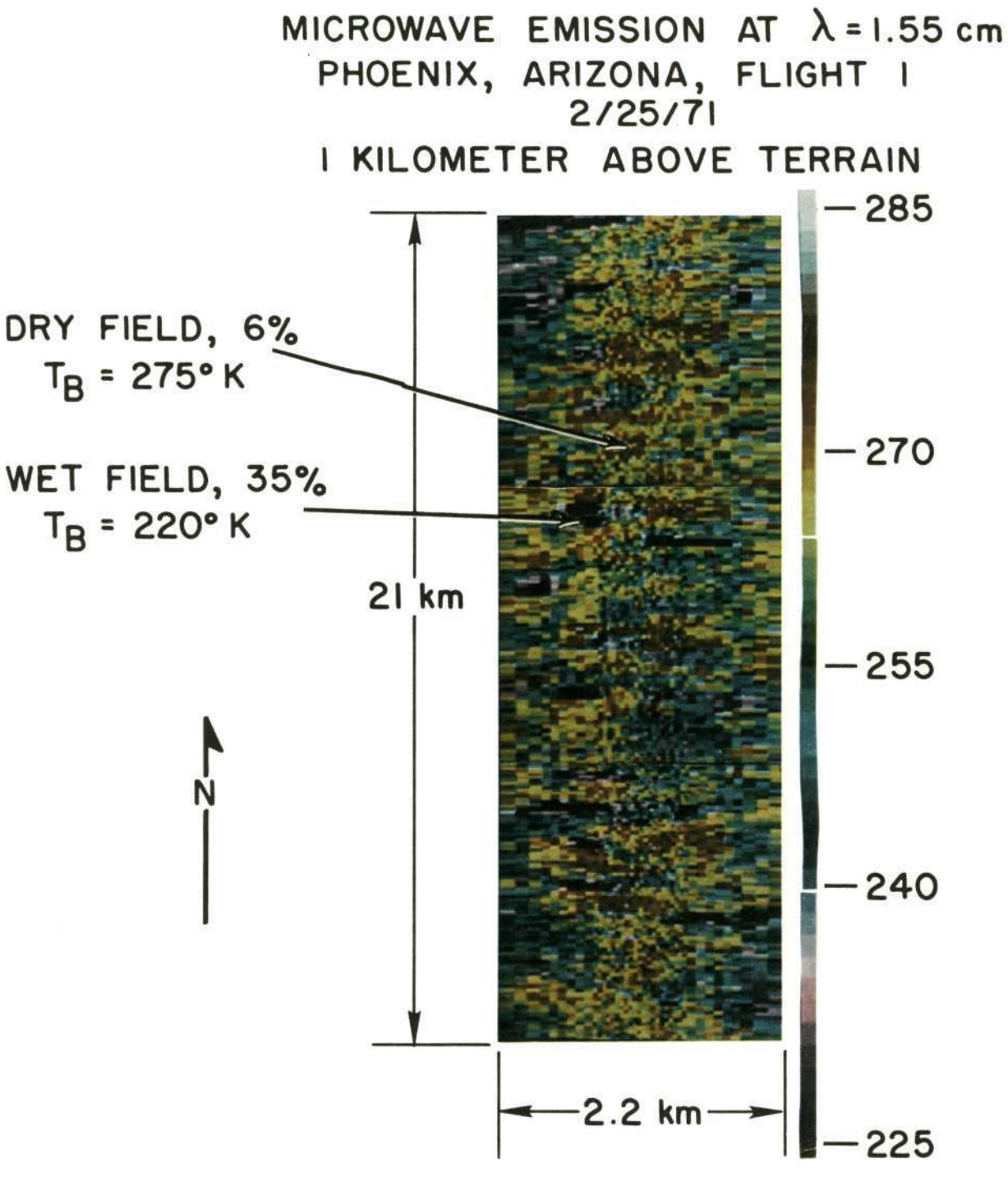

Figure 8 19.35 GHz image of an agricultural area near Phoenix, Arizona

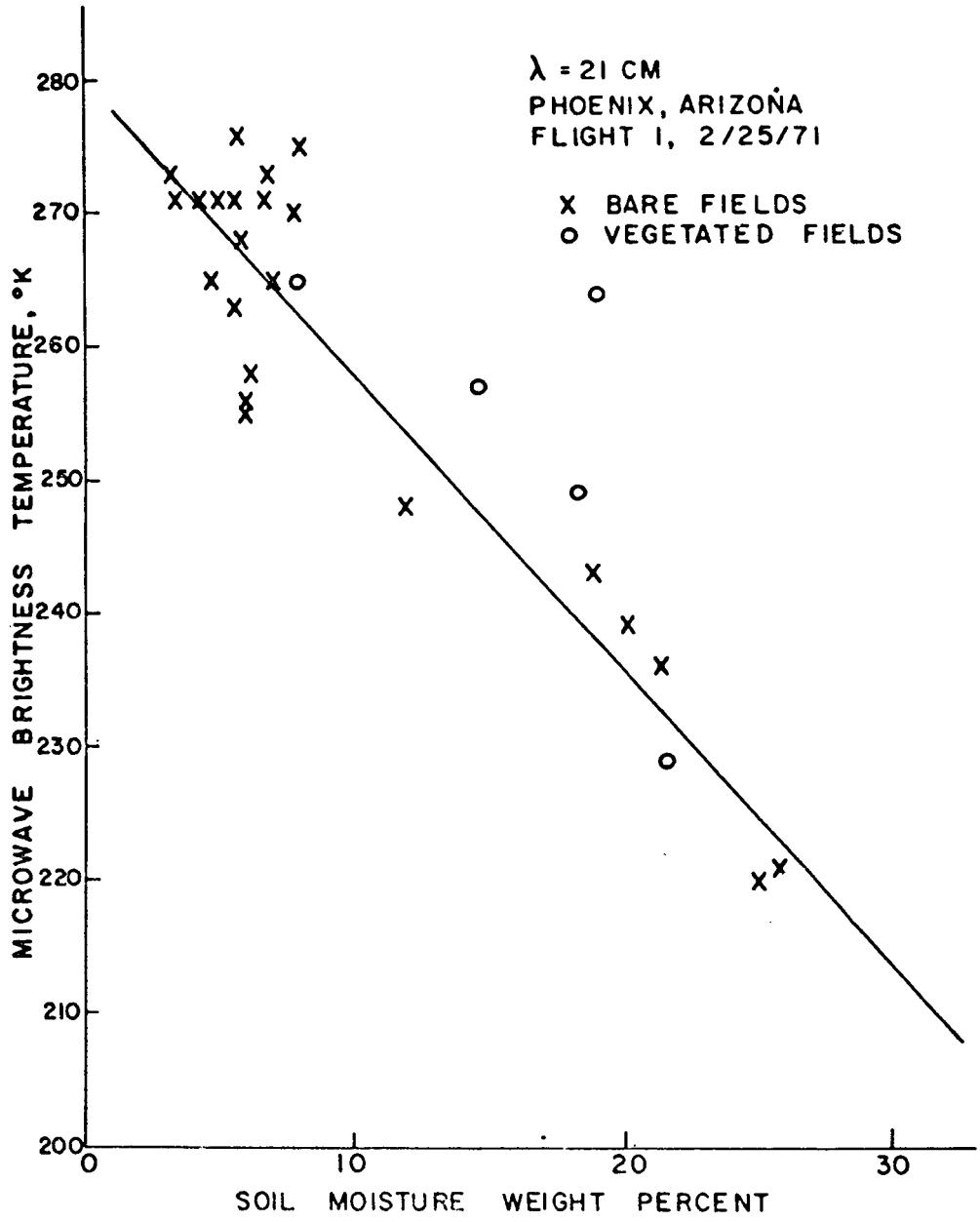

Figure 9 Radiometric temperature vs % soil moisture, by weight at 1.42 GHz

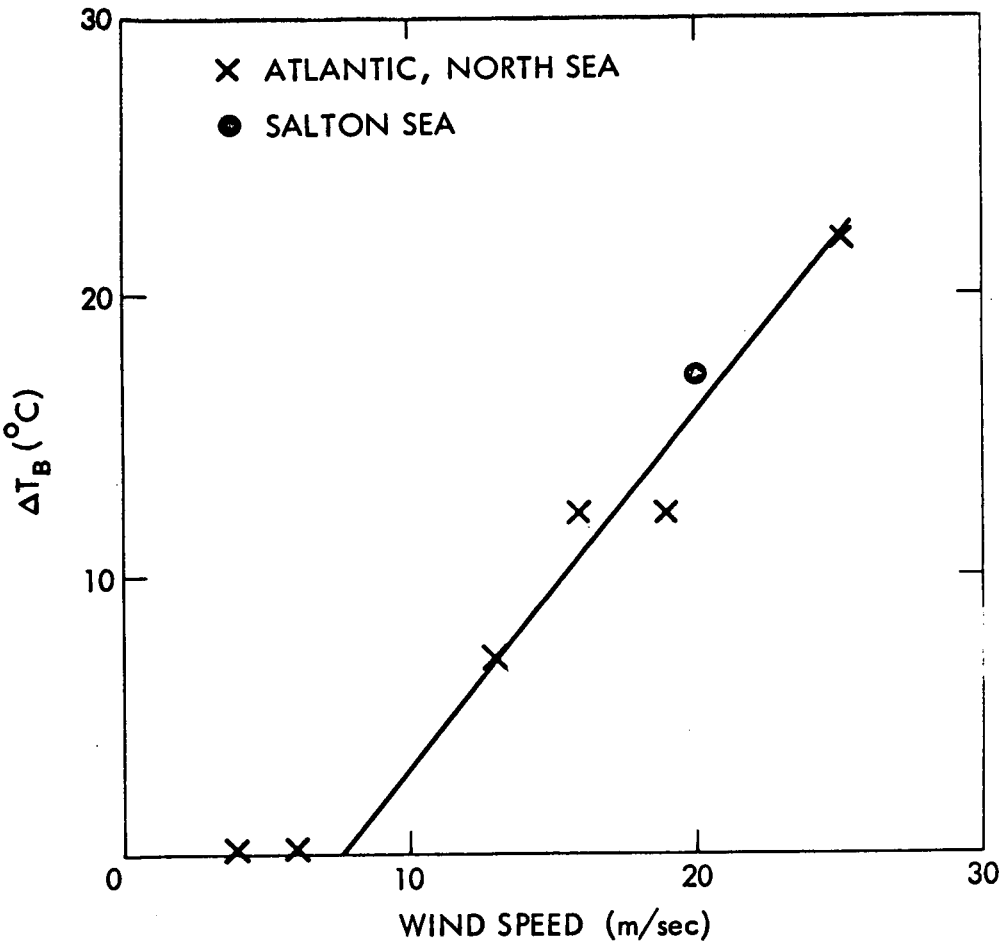

Figure 10

Change in brightness temperature vs wind speed at the sea surface at 19.35 GHz

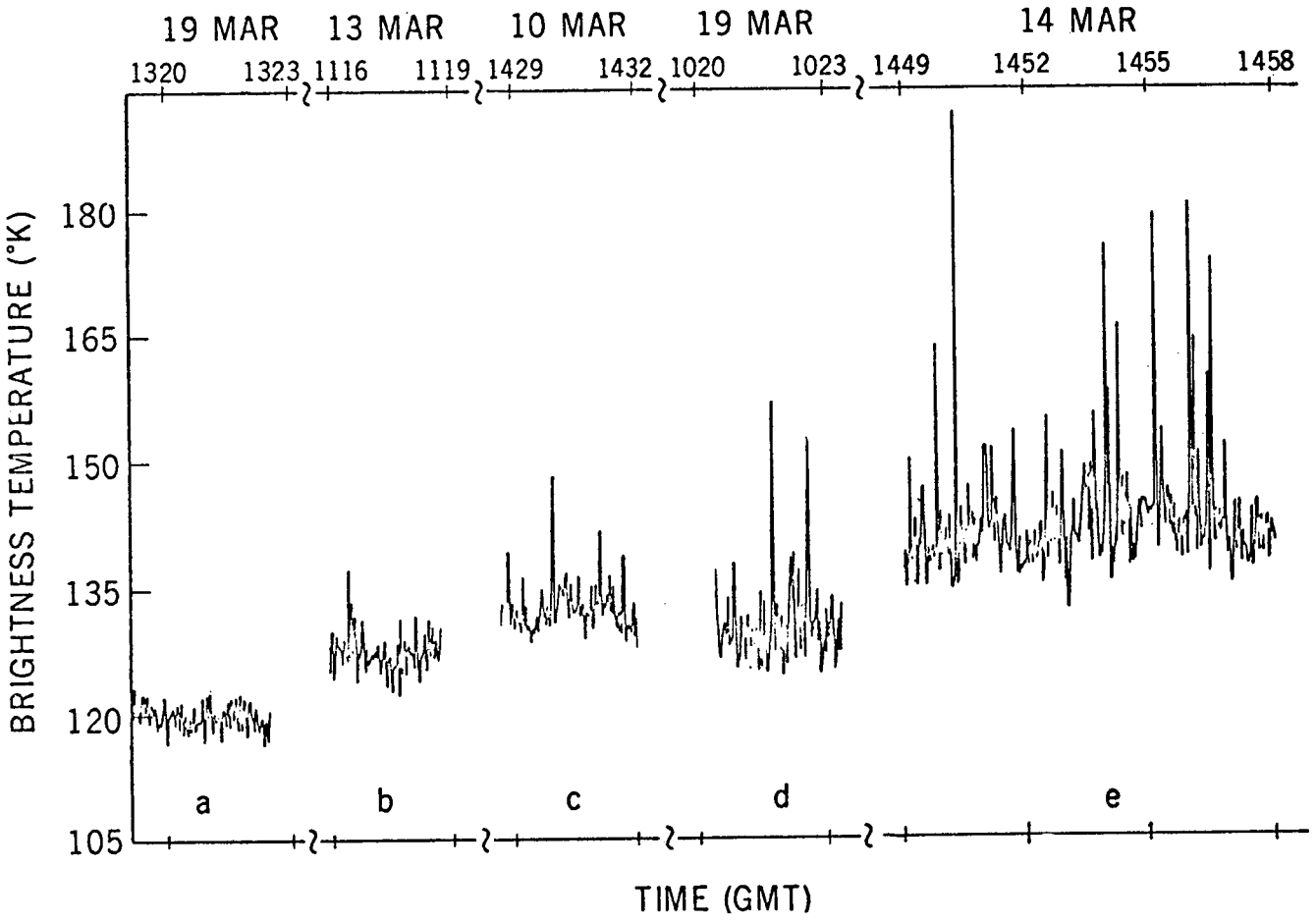

Figure 11 Radiometric temperature records of the sea at 19.35 GHz for various surface wind speeds, increasing from left to right

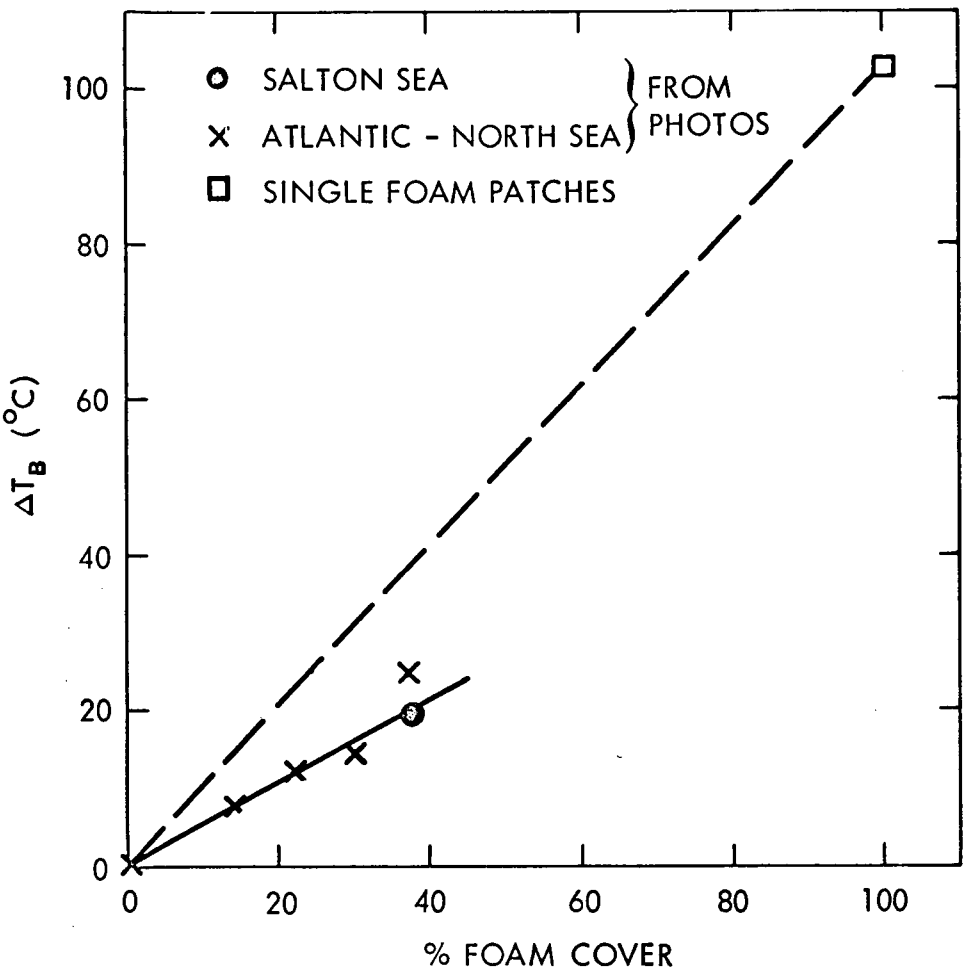

Figure 12

Radiometric temperature of the sea as a function of percent foam cover, as determined by photogrametry